

Unraveling the Lithium/Sodium-Ion Diffusion Mechanism in Alloyed Phosphides for Lithium/Sodium Storage

Qiang Wang,^{*,†} Hongfei Zheng,[†] Yinhua Ma, Yiming Zhao, Wei Ran, Jianfang Chen, Qiwei Wang, Liping Yang, Qingshui Xie, Chaoling Wu, Wei Liu,^{*} and Lei Shen^{*}



Cite This: *J. Phys. Chem. C* 2024, 128, 8571–8579



Read Online

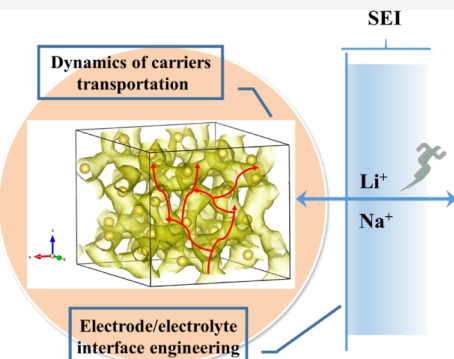
ACCESS |

Metrics & More

Article Recommendations

Supporting Information

ABSTRACT: Phosphorus is a promising candidate for high energy density lithium/sodium-ion batteries due to its high capacity. However, the dynamics of carrier shuttling in the alloyed phosphorus anode are quite complex due to the multiple phase transitions during the lithiation/sodiation process. Here, we identify Li(Na)P and Li(Na)₃P as stable phases from both ex situ and in situ X-ray diffraction measurements of black phosphorus (BP). Our results regarding the dynamics of lithiation/sodiation indicate that the entire reaction could be limited by sluggish lithium/sodium ion migration in the stable phases, Li(Na)P and Li(Na)₃P, supported by *ab initio* molecular dynamics (AIMD) simulations. Additionally, Li₃P has higher activation energies and correspondingly lower ion conductivity than LiP, making it the key role in the whole dynamics of lithium-ion transport during the lithiation process. In comparison, the dynamics of sodiation exhibit quite active behavior due to lower energy barriers for sodium-ion transport. However, the electrochemical performance of sodium-ion batteries suffers from a large charge transfer resistance at the electrode/electrolyte interface due to the generation of corrosive Na₃P. Therefore, the construction of a stable solid electrolyte interphase (SEI) is crucial to improving the electrochemical performance of phosphorus anodes.



1. INTRODUCTION

Alloy-type anodes have been increasingly considered promising candidates for lithium/sodium-ion batteries due to their high energy density compared with traditional graphite or hard carbons.^{1–4} Silicon/silica, on the other hand, has been developed as a high-capacity, cyclable anode material for lithium-ion batteries in the commercial market.^{5–8} Recently, alternative materials, such as phosphorus and tin, have attracted significant attention due to their ability to make a compromise between high energy density and capacity loss.^{9–12} In principle, silicon/silica would be swollen to form a porous structure and gradually infiltrated by the electrolyte to generate a more solid electrolyte interphase (SEI), which disrupts the electrical contact and forms dead silicon, subsequently causing capacity fading.¹³ Phosphorus, in particular, has a medium capacity between silicon and tin and can store Li/Na/K for rechargeable batteries, making it a key focus for lithium/sodium-ion battery research.^{14,15} Layered black phosphorus (BP) is a noteworthy material that can be exfoliated into two-dimensional phosphorene, facilitating fast lithium/sodium-ion insertion for the electrochemical discharge/charge process.^{16,17}

Recently, black phosphorus, ball-milled with graphite and polyaniline (PANI), has delivered reversible capacities under different rate capabilities and long cycle abilities.¹⁸ These improvements are attributed to the restraining effect of the

heterojunction between BP and graphite and the coated PANI. Another strategy that has made progress is the combination of red phosphorus with bismuth (Bi) as the raw material rather than expensive BP due to the complicated synthesis process.¹⁹ The heterojunction between red phosphorus and Bi was ball-milled with graphite, which gave rise to better dynamics of lithium-ion transportation in galvanostatic intermittent titration technique (GITT) examination than that of pristine red phosphorus.^{20,21} However, during the discharge/charge process, both lithium and sodium phosphides undergo large-volume swelling and pulverization, leading to extraordinary exhaustion of electrolytes and introducing an increase of solid electrolyte interphases and capacity loss.¹¹ Fully formed SEI films have high lithium-ion conductivity and negligible electronic conductivity. Essentially, these electrochemical behaviors contribute to the kinetic degradation of lithium/sodium-ion transportation in the alloying process. To improve this, the stable SEI can be strengthened by electrolyte additives,^{22,23} novel binders,^{24–27} and surface coatings.²⁸

Received: February 24, 2024

Revised: April 23, 2024

Accepted: May 9, 2024

Published: May 17, 2024



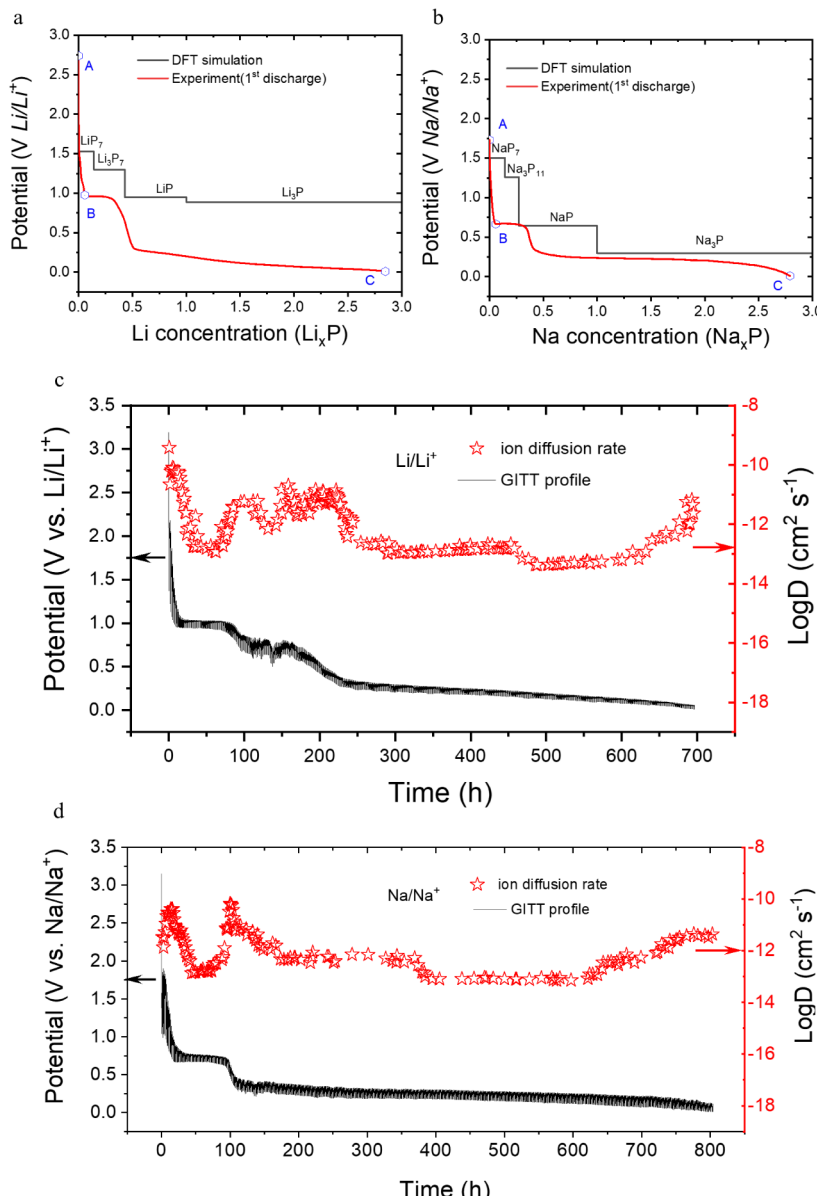


Figure 1. Electrochemical characterization of lithiation/sodiation of BP: galvanostatic discharge curves obtained by both experiments (the first cycle) and first-principle calculations (a, b), and ion-diffusion coefficient calculated by GITT plot (c,d).

Coating substances usually include carbon and derivatives,^{29,30} fast ion-conductive compounds,³¹ and electron-conductive polymers.^{18,32} In addition, many previous researchers have paid much attention to the insertion and diffusion processes in phosphorus during the initial stage of lithiation/sodiation.^{33–35} So far, only a few reports have been conducted on ion transportation during subsequent alloying processes.³⁶

The observed issues in the phosphorus anode, such as voltage hysteresis and poor rate capability, underscore the need to better understand lithium/sodium-ion diffusion dynamics and their improvement. To this end, our study aims to identify the mediated lithium/sodium phosphides during the alloying process using *in situ* and *ex situ* X-ray diffraction (XRD) techniques. Additionally, we employ *ab initio* molecular dynamics (AIMD) and climbing-image nudged elastic band (CINEB) techniques to reveal the atomic-level mechanism of phosphorus alloying. Our results demonstrate the varied dynamics of lithium–sodium-ion interaction with BP via an

alloying mechanism, providing an effective strategy for investigating alkali metal ion transportation in alloy-type anode materials. Furthermore, this research offers insights into the design of high-rate-capacity and high-capacity-durability alloy-type anodes for lithium/sodium storage.

2. MATERIALS AND METHODS

2.1. Materials and Electrochemical Examinations.

Black phosphorus (BP) was purchased from commercial markets and used without further purification. Bulk BP was first crushed into microscale particles and then ground in a mortar for further testing and characterization. Electrochemical experiments were carried out by fabricating CR2032-type coin cells with lithium metal counter electrodes in an Ar-filled glovebox. Electrode films were prepared using 70 wt % active material, 20 wt % acetylene black, and 10 wt % polyvinylidene fluoride (PVDF) binder. The electrolyte was 1 mol L⁻¹ LiPF₆ in ethylene carbonate (EC) and dimethyl carbonate (DMC),

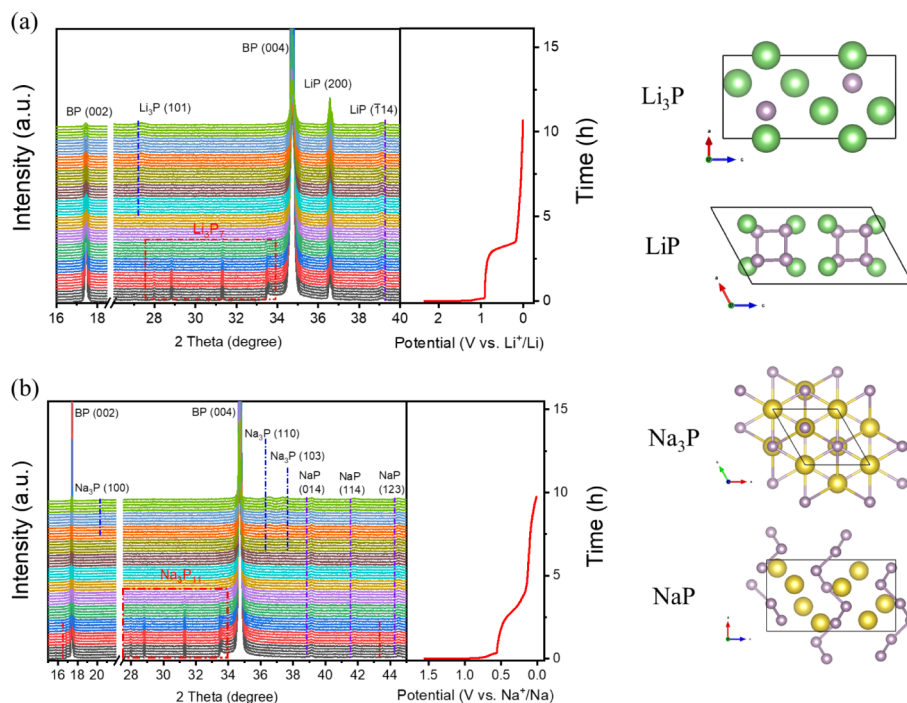


Figure 2. In situ XRD characterization of the lithiation/sodiation of BP: In situ XRD measurements in the range of 10–40° for Li (a) and 10–45° for Na half-cell (b). The green, yellow, and purple spheres represent lithium, sodium, and phosphorus atoms.

EC/DMC = 1:1 vol % for the Li-ion cell, and 1.0 M NaClO₄ dissolved in an ethylene carbonate/dimethyl carbonate (EC/DMC, 1:1 by vol.) solution with 5 wt % fluoroethylene carbonate (FEC) for the Na-ion cell. Galvanostatic discharge/charge tests were performed on a Land battery test system CT-2001A (Wuhan, China) versus a Li counter electrode. For the GITT examination, the cell was discharged at a current of 50 mA g⁻¹ for 30 min, followed by open-circuit relaxation for 60 min during each pulse. Then, data analysis of lithium/sodium ions diffusion was performed using Website tools of GITT V2 developed by Editor Tan (<http://www.upub.online/gitt.html>). Electrochemical impedance spectroscopies (EIS, 100 kHz to 0.01 Hz) were collected on the Parstat 3000-DX electrochemical workstation.

To precisely characterize the alloying phase emerging in the discharge process, alloying phases in the lithiation/sodiation of BP were characterized by both in situ XRD and ex situ XRD measurement. In situ XRD experiments were performed on a Bruker D8-A2S (Cu K_α radiation, 40 kV and 40 mA) with a current of 100 mA g⁻¹ between 0.01 and 3.0 V for the initial cycle. Meanwhile, ex situ X-ray diffraction (XRD) was also characterized on the aforementioned XRD device at a scan rate of 1.2° min⁻¹ within a 2θ range from 10 to 90°, which could exhibit more structural information on alloying phases at different depths of discharge (DOD). Correspondingly, the morphology of the electrode in each status of discharge was also observed by a scanning electron microscope (SEM) of Hitachi SU-70.

2.2. Theoretical Calculation. First-principles calculations were performed using density functional theory (DFT) with the exchange-correlation functional of the generalized gradient approximation (GGA) of Perdew, Burke, and Ernzerhof (PBE) method,³⁷ which was implemented in the Vienna ab initio simulation package (VASP).³⁸ The cutoff energy of the plane wave was set to 500 eV, and the convergence threshold for self-

consistent iteration was 10–5 eV. The structural configurations were relaxed until the residual forces were below 0.03 eV/Å with a 6 × 6 × 6 k-point grid centered at the k-point. All initial crystal structures of BP and lithium/sodium phosphides were obtained from the Inorganic Crystal Structure Database³⁹ and Materials Project.⁴⁰

Lithium/sodium ion transportation was calculated by AIMD in an NVT ensemble with a Nosé–Hoover thermostat⁴¹ in the temperature range of 1400–2000 K. Supercells containing the 2 × 2 × 1 conventional cell and a Γ-centered 1 × 1 × 1 k-mesh were used. The calculation procedure was first heated to the given temperature, subsequently equilibrated, and the last diffusivity converged, as described in more detail.⁴² All AIMD calculations were carried out with a time step of 2 fs for a total of 120 ps, and the diffusivities were studied based on mean square displacement (MSD).⁴³ Subsequently, a converged Arrhenius plot was plotted to obtain the activation energy (E_a).⁴⁴

For the analyses of the lithium/sodium-ion transportation, pymatgen diffusion was used.⁴⁵ Pymatgen diffusion is implemented in Python Materials Genomics⁴⁶ (pymatgen, <http://pymatgen.org/>). Meanwhile, the diffusion of Li ions was also studied in lithium phosphide to explore the atomistic lithium-ion diffusion mechanism. The climbing-image nudged elastic band (CI-NEB) method⁴⁷ was employed to search for the minimum energy paths (MEP) for Li diffusion. The electronic conductivity over relaxation time (σ/τ) was calculated by solving the Boltzmann transport equation (BTE) of electrons based on the constant relaxation time (τ) approximation (CRTA) implemented in the BoltzTrap code.⁴⁸ The final σ value was obtained by multiplying the output data of BoltzTrap, σ/τ , and calculated by the deformation potential theory^{49,50} (see Supporting Information for detailed description).

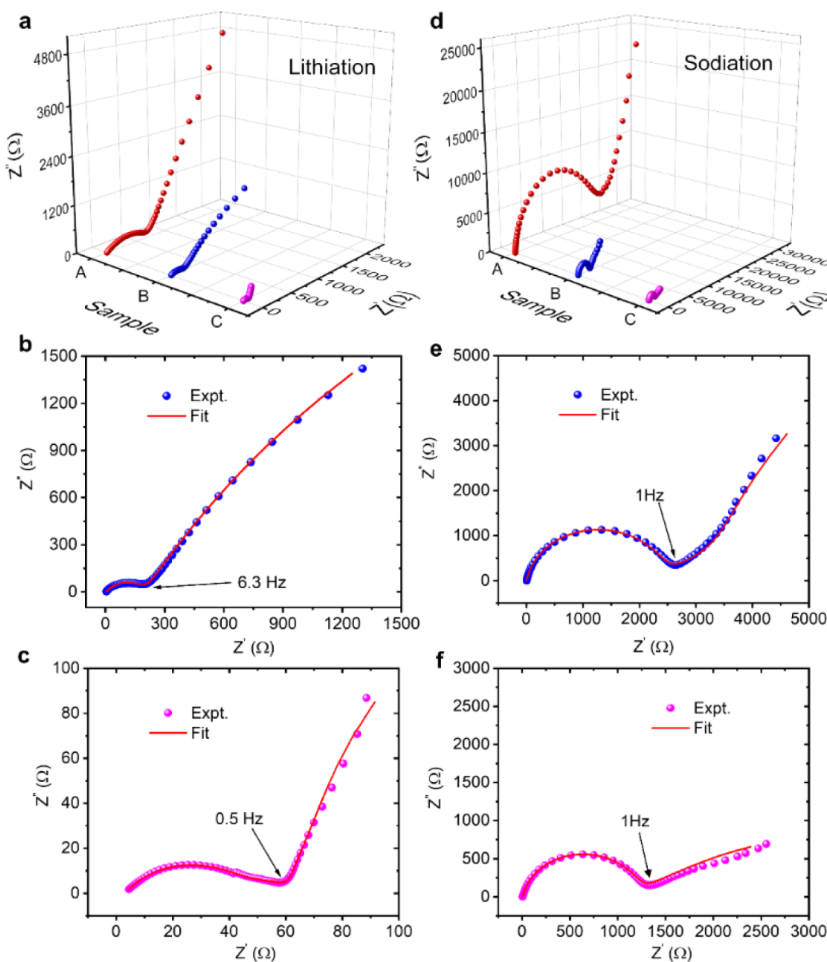


Figure 3. EIS profiles of BP lithiation/sodiation at the A, B, and C stages (a,d); the experimental data and fitted EIS profiles at the B stage (b, e) and C stage (c, f); a to c for lithiation and d to f for sodiation.

3. RESULTS AND DISCUSSION

3.1. Electrochemical Behaviors of BP Alloying with Li/Na. Figure 1 illustrates the initial galvanostatic discharge/charge curves of lithium/sodium half-cells to understand the electrochemical behaviors of the BP alloying process. The discharge/charge profiles' potentials (red line) correspond to those calculated (black line) for $\text{Li}_3\text{P}_7(\text{Na}_3\text{P}_{11})$, $\text{LiP}(\text{NaP})$, and $\text{Li}_3\text{P}(\text{Na}_3\text{P})$ by first-principles calculation (Figure 1a,b), indicating good agreement between the DFT calculated and electrochemical examination. Notably, these potential plateaus approach good agreement between electrochemical testing and first-principles calculation, except for the final product of Li_3P . Additionally, the dynamics of Li/Na diffusivity (Figure 1c,d) show a downward trend and reach a minimum corresponding to the potential plateaus of $\text{LiP}(\text{NaP})$ and $\text{Li}_3\text{P}(\text{Na}_3\text{P})$. This coincidence indicates that Li/Na ions diffusion in these corresponding alloying phases plays a key role in impacting the GITT examination.

Furthermore, the morphology of the electrodes at the A, B, and C points in Figures 1a,b is illustrated to explore the evolution of the surface and interface between the electrode and electrolyte, as shown in Figure S1. BP's surface evolution during discharge displays the typical "expansion and pulverization"^{1,51} failure of alloyed-type anodes. Specifically, lamellar bulk BP (A, Figure S1a, b) partially swells and pulverizes to form a foam-like surface (Figure S1c), and many

cracks occur on the surface of the leftover BP (Figure S1d) during lithiation at the B stage. At the final C stage, the foam-like lamellae exhibit more expansion than before (Figure S1g), and large nanoscale particles can be observed on the surface, which might be new alloying phases that emerged (Figure S1h). Unfortunately, the sodiation process displays many micro- or nanofibers on the surface at the B stage (Figure S1e, f) and suffers intensive corroding through large pores on the electrode's surface (Figure S1i, j), where many microspheres of new nanoscale particles can be observed nearby.

The evolution of phase changes during BP lithiation/sodiation was characterized using in situ XRD, and the results are plotted in Figure 2. During the lithiation process, the emergence of the alloying phases Li_3P_7 , LiP , and Li_3P was observed (Figure 2a). Interestingly, LiP (200) remained stable throughout the discharge process, while the emergence of Li_3P_7 and Li_3P (101) was due to the potential plateau in the discharge curves. Li_3P_7 disappeared below the first potential plateau (around 1 V). Similarly, during the sodiation of BP, stable alloying phases of NaP and Na_3P were observed, along with a trace of Na_3P_{11} (Figure 2b). As shown in Figure S2, ex situ XRD examination during the entire discharge/charge process (A, B, and C points in Figure 1ab) only illustrated the trail of the final Li_3P and Na_3P during the discharge (C) stages. Other lithiation/sodiation of BP^{34,52} indicated a transformation from amorphous Li_xP (Na_xP) to crystallized Li_3P

Table 1. Resistance and Ion-diffusion Coefficient Results of Fitted EIS Profiles

	lithiation			sodiation		
	R_e (Ω)	R_{sei} (Ω)	D_{Li} ($\text{cm}^2 \text{s}^{-1}$)	R_e (Ω)	R_{sei} (Ω)	D_{Na} ($\text{cm}^2 \text{s}^{-1}$)
stage B	2.913	199.2	6.64×10^{-12}	4.33	2518	8.36×10^{-12}
stage C	2.825	52.25	2.27×10^{-11}	3.9	1151	8.96×10^{-12}

and Na_3P at the final stage, while delithiation of the crystalline Li_3P was difficult during the next charge process. These experiments showed good agreement with our ex situ XRD results of Li_3P and Na_3P in the recharge state (Figure S2). Considering the lower current density in ex situ XRD examination, the crystallization of Li_3P and Na_3P would be much slower and less in weight ratio than in the in situ XRD testing. A higher current density in in situ XRD testing would stimulate the generation and crystal growth of $\text{Li}(\text{Na})\text{P}$ and $\text{Li}(\text{Na})_3\text{P}$ due to a higher gradient of Li/Na ions.

Figure 3a,b presents the results of electrochemical impedance spectroscopy (EIS) tests conducted at various discharge stages (points A, B, and C in Figure 1a,b), which were aimed at observing the electrochemical kinetics of BP lithiation/sodiation. The EIS profile was analyzed using Zsimpwin software, and the results are presented in Figure 3b,c for lithiation and Figure 3e,f for sodiation. These results were fitted and analyzed to calculate the resistance of the solid electrolyte interface (SEI), R_{sei} , and the ion-diffusion coefficient, D . The computed values of R_{sei} and D are presented in Table 1. The equivalent circuit and a detailed explanation are found in Figure S3. Notably, R_{sei} decreased from stage B to C in both lithiation and sodiation, while the lithium/sodium ion-diffusion coefficient showed a slight increase. These coefficients were found to be in excellent agreement with the results of the GITT examination.

In addition, we also computed the electron conductivity of lithium/sodium phosphides through a DFT calculations, as demonstrated in Table S1 and Figure S4. The results showed that there was a significant disparity in electron conductivity between LiP and Li_3P , regardless of their P-type or N-type semiconductivity. This finding is consistent with experimental data indicating lower electron conductivity in Li_3P .⁵² This suggests that fluctuations in the active materials of the electrode would have a minimal impact on the overall electrical contact of the electrode system, owing to the inclusion of conductive carbon materials, even during the transformation from crystalline BP to amorphous lithium/sodium phosphides.

3.2. Lithium/Sodium-Ion Diffusion in Alloyed Phosphides. The irreversible transformation of amorphous Li_xP (Na_xP) into crystalline $\text{Li}(\text{Na})\text{P}$ and $\text{Li}(\text{Na})_3\text{P}$ results in a lower diffusion rate of lithium/sodium ions in crystallized phosphides compared to that in amorphous phosphides. This tardiness in lithium/sodium ion exchange during electrochemical reactions could be due to the accumulation of crystalline phosphides during cycling. To study the migration of lithium/sodium ions in stable lithium/sodium phosphides, AIMD simulations were conducted using supercells of $2 \times 2 \times 1$. The ion diffusion pathways in these lattices are illustrated in Figure 4, along with the activation energy E_a , which was plotted using the Arrhenius equation. For this calculation, the AIMD simulation was performed at a higher temperature range (1400–2000 K) than that for a fast ion conductor (600–1200 K)⁴³ to ensure better accuracy of ion transportation,⁴⁴ as shown in the mean square displacement (MSD) plot in Figure S5. The crystalline nature of these lithium/sodium phosphides

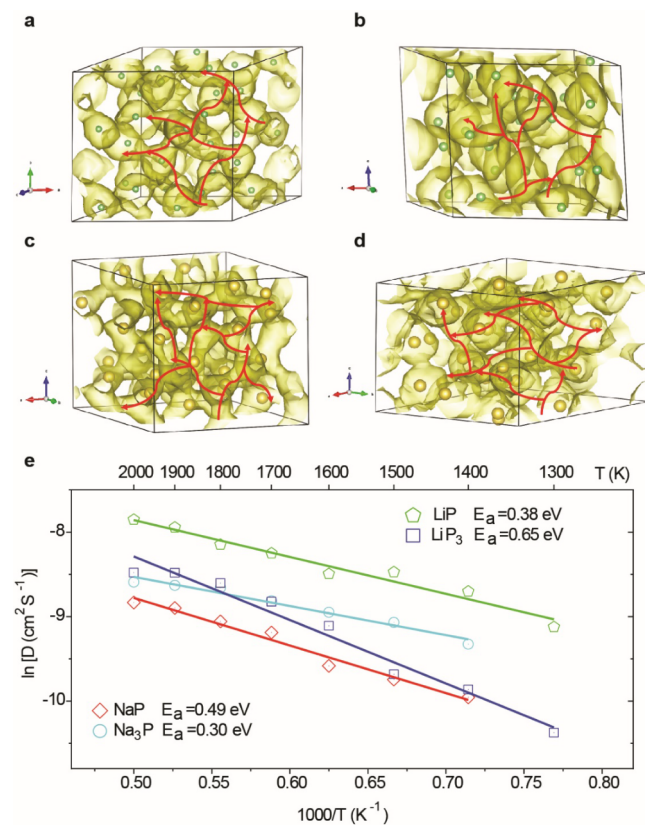


Figure 4. AIMD calculation and analysis of lithium/sodium phosphides: visualization of the lithium-ion migration path in $2 \times 2 \times 1$ supercells of $\text{Li}(\text{Na})\text{P}$ (a, c) and $\text{Li}(\text{Na})_3\text{P}$ (b, d), and Arrhenius equation plot (e). The green and yellow spheres represent the lithium and sodium atoms, respectively.

was analyzed using the pair distribution function, as shown in Figure S6, where a second-neighbor peak in M-M, M-P, and P-P (M: Li/Na) profiles could be observed. Moreover, the probability density of Li/Na, as shown in Figure 4a–d, illustrated a connection with the adjacent Li/Na atoms and formed a network in the lattice, facilitating Li/Na migration. This network is depicted by red arrows in the figure. The coordination between adjacent Li/Na atoms indicates the existence of a diffusion pathway in the crystal lattice, which enables Li/Na to hop and transport.

Figure 4e displays the Arrhenius plots from the AIMD simulation. Profiles of $\ln D - 1/T$ were fitted and showed minor errors for activation energy E_a plotted by the Arrhenius equation (Figure S7). LiP exhibited a much lower E_a compared to Li_3P , resulting in fast lithium-ion migration at the initial stage and a dramatic decrease at the Li_3P stage. This was consistent with the degradation of Li-ion diffusion in the GITT examination at the final stage (Figure 1c). Interestingly, the AIMD simulations showed better dynamics of sodiation/desodiation than lithiation/delithiation. However, slower dynamics of sodium-ion diffusivity could be attributed to a larger resistance of charge transfer (R_{ct}) at the interface and

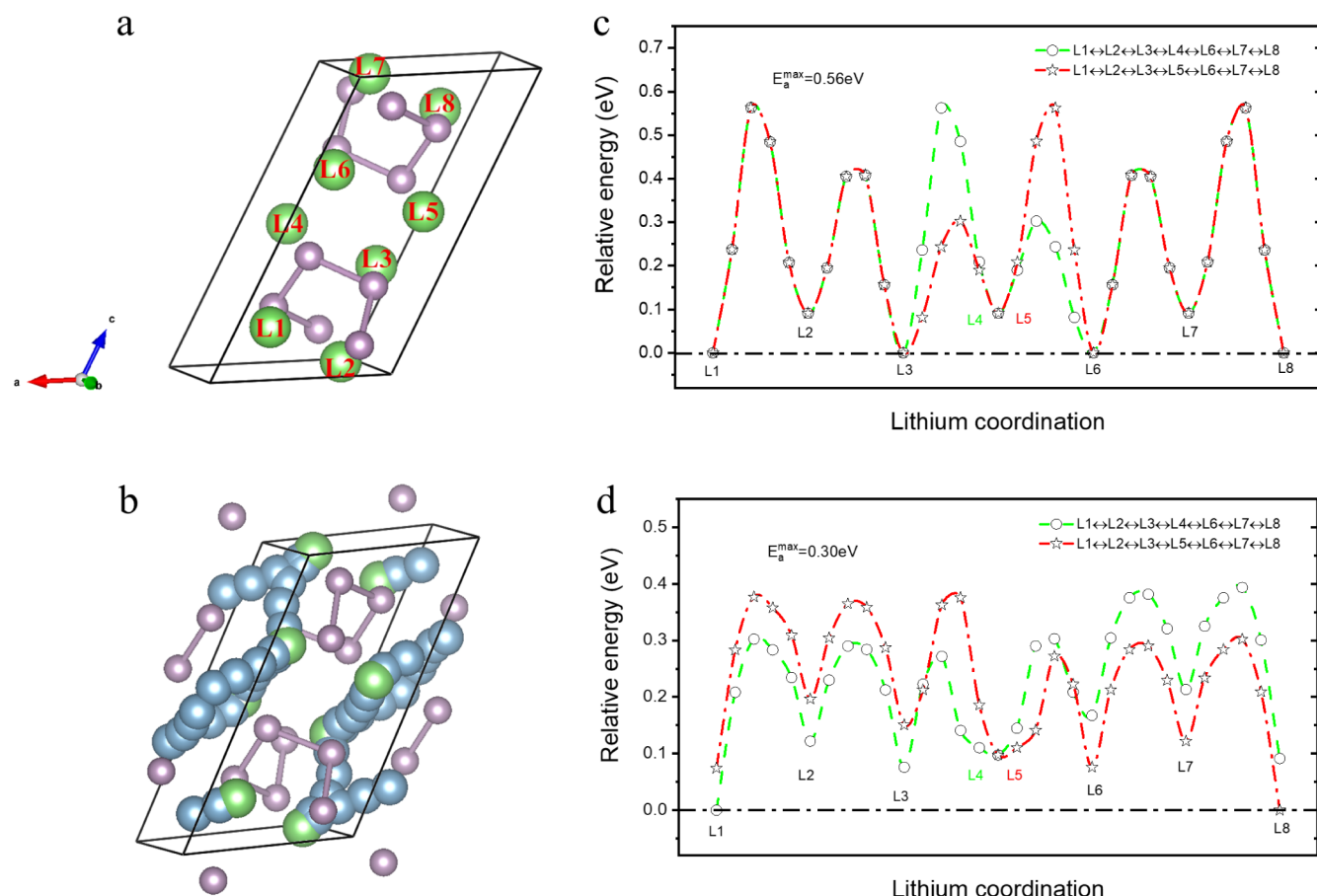


Figure 5. CINEB calculation and analysis of lithium phosphide. Lithium denoted (a) and migration path in LiP(b) and the corresponding energy barriers plotted by single vacancy (c) and divacancy mechanism (d). The green and purple spheres represent lithium and phosphorus atoms, respectively. The blue sphere represents the lithium diffusion path in the unit cell of the LiP crystal structure.

more corrosion on the surface of electrodes than that of lithiation, as confirmed by degradation on the surface of the electrode and EIS testing results (Figures S1 and 2).

LiP was used to demonstrate the atomic mechanism of lithium-ion diffusion in the phosphide alloying phases. The lithium-ion and probability pathway of migration were investigated by CINEB for LiP, as shown in Figure 5a,b. The results showed that lithium-ion transport demonstrated divacancy migration energetically, which delivered a maximum activation energy of 0.30 eV, compared with 0.56 eV in the single vacancy model calculation (Figure 5c,d). This diverse activation energy in two types of mechanisms could also be observed in LiCoO_2 and NaCoO_2 cathode materials⁵³ in which lithium/sodium atoms were energetically favorable to immigrate by the divacancy mechanism. Furthermore, energy barriers for the divacancy model approached the activation energy of the aforementioned AIMD simulation (0.38 eV), where the discrepancy could have originated from time-dependent ion diffusion while that of static computation in the NEB method.⁵⁴

The AIMD or NEB methods for ion transportation calculation are quite exhaustive of computing resources and are therefore expensive for large-scale materials screening of fast ion conductors.⁵⁵ The bond valence (BV) method can also be applied in crystallography to estimate energy barriers and possible ion transportation pathways by bond length and charge transfer around anion atoms.⁵⁶ In this study, the Bader charge was computed to evaluate ion transportation in the

alloying phases of the lithiation and diatomase ionization of BP, as shown in Table 2. Charge transfer among these

Table 2. Formation Energy and Bader Charge Calculation of Lithium/Sodium Phosphides

	formation energy (eV)	Bader charge		
		Li	Na	P
LiP	-0.55	-0.32	-	+0.32
Li_3P	-0.72	-0.4	-	+1.2
NaP	-0.41	-	-0.3	+0.3
Na_3P	-0.35	-	-0.37	+1.11

phosphides follows the order $\text{Li}_3\text{P} > \text{Na}_3\text{P} > \text{LiP} > \text{NaP}$, and these electron interactions are also confirmed by charge density difference calculation, as shown in Figure S8. Considering the formation energy of these alloying phases, Li_3P displayed more stability in thermodynamics than LiP, NaP, and Na_3P , which indicates that Li_3P is energetically favorable to crystallize from amorphous Li_xP but it is difficult to break up the Li–P bond for lithium-ion migration.

4. CONCLUSION

We identified intrinsic alloying phases in Li/Na phosphides and revealed the atomic mechanisms of lithium/sodium ion transportation during the discharge process. Our results indicate that the sluggish dynamics of lithium migration in

crystalline Li₃P could be the key to improving the kinetics of electrochemical performance. Additionally, the presence of corrosive Na₃P at the interface led to a significant charge-transfer resistance, which harmed the electrochemical performance compared to the lithiation of black phosphorus. This research explores the pristine dynamics of lithium/sodium ion diffusion in crystallized phosphides, which could play a crucial role in the kinetics of electrochemical reactions at the anode side. The strategies discussed in this study, including composition/structure rational design and surface modification, could shed light on improving black phosphorus to achieve high-energy density and long cycle-ability.

■ ASSOCIATED CONTENT

Supporting Information

The Supporting Information is available free of charge at <https://pubs.acs.org/doi/10.1021/acs.jpcc.4c01211>.

Final σ value obtained by multiplying the output data of BoltzTrap, σ/τ , and calculated by the deformation potential theory([PDF](#))

■ AUTHOR INFORMATION

Corresponding Authors

Qiang Wang – School of Materials and Energy, Southwest University, Chongqing 400715, PR China;  [orcid.org/0000-0002-7396-0323](#); Email: wysnu@swu.edu.cn

Wei Liu – Institute of New-Energy and Low-Carbon Technology, Engineering Research Center of Alternative Energy Materials & Devices, Ministry of Education, Sichuan University, Chengdu 610065, PR China;  [orcid.org/0000-0003-1608-7270](#); Email: weiliu@scu.edu.cn

Lei Shen – Department of Mechanical Engineering, National University of Singapore, Singapore 117575, Singapore;  [orcid.org/0000-0001-6198-5753](#); Email: shenlei@nus.edu.sg

Authors

Hongfei Zheng – College of Materials, Xiamen University, Xiamen, Fujian 361005, PR China

Yinhua Ma – School of Materials and Energy, Southwest University, Chongqing 400715, PR China

Yiming Zhao – Department of Mechanical Engineering, National University of Singapore, Singapore 117575, Singapore;  [orcid.org/0000-0002-3921-1900](#)

Wei Ran – School of Materials and Energy, Southwest University, Chongqing 400715, PR China

Jianfang Chen – School of Materials and Energy, Southwest University, Chongqing 400715, PR China

Qiwei Wang – School of Materials and Energy, Southwest University, Chongqing 400715, PR China

Liping Yang – School of Materials and Energy, Southwest University, Chongqing 400715, PR China

Qingshui Xie – College of Materials, Xiamen University, Xiamen, Fujian 361005, PR China;  [orcid.org/0000-0003-2105-6962](#)

Chaoling Wu – Institute of New-Energy and Low-Carbon Technology, Engineering Research Center of Alternative Energy Materials & Devices, Ministry of Education, Sichuan University, Chengdu 610065, PR China;  [orcid.org/0000-0001-7629-9748](#)

Complete contact information is available at: <https://pubs.acs.org/10.1021/acs.jpcc.4c01211>

Author Contributions

[†]Q.W. and H.Z. contributed equally to this work.

Notes

The authors declare no competing financial interest.

■ ACKNOWLEDGMENTS

This work was financially supported by the Chongqing Natural Science Foundation General Project (Grant No. CSTB2023NSCQ-MSX0769); National Key Research and Development Program of China (2022YFE0135900); the Open Project of Engineering Research Center of Alternative Energy Materials & Devices, Ministry of Education, Sichuan University (Grant No. AEMD202209); and the Chongqing Municipal Training Program of Innovation and Entrepreneurship for Undergraduates (Grant Nos. S202210635075, X202310635557, ZSM202318). In addition, Y.M.Z. would like to gratefully acknowledge the support of the China Scholarship Council (No. CSC202104910079). We would also like to appreciate Dr. Chunli Wang and Dr. Weilong Kong for their beneficial discussions. Received: ((will be filled in by the editorial staff)) Revised: ((will be filled in by the editorial staff)) Published online: ((will be filled in by the editorial staff))

■ REFERENCES

- (1) Fang, L.; Bahlawane, N.; Sun, W.; Pan, H.; Xu, B.; Yan, M.; Jiang, Y. Conversion-Alloying Anode Materials for Sodium Ion Batteries. *Small* **2021**, *17* (37), 2101137.
- (2) Zhang, H.; Hasa, I.; Passerini, S. Beyond Insertion for Na-Ion Batteries: Nanostructured Alloying and Conversion Anode Materials. *Adv. Energy Mater.* **2018**, *8* (17), 1702582.
- (3) Lao, M.; Zhang, Y.; Luo, W.; Yan, Q.; Sun, W.; Dou, S. X. Alloy-Based Anode Materials toward Advanced Sodium-Ion Batteries. *Adv. Mater.* **2017**, *29* (48), 1700622.
- (4) Obrovac, M. N.; Chevrier, V. L. Alloy Negative Electrodes for Lithium Batteries. *Chem. Rev.* **2014**, *114* (23), 11444–11502.
- (5) Ge, M.; Cao, C.; Biesold, G. M.; Sewell, C. D.; Hao, S. M.; Huang, J.; Zhang, W.; Lai, Y.; Lin, Z. Recent Advances in Silicon-Based Electrodes: From Fundamental Research toward Practical Applications. *Adv. Mater.* **2021**, *33* (16), 2004577.
- (6) Guo, J.; Dong, D.; Wang, J.; Liu, D.; Yu, X.; Zheng, Y.; Wen, Z.; Lei, W.; Deng, Y.; Wang, J.; Hong, G.; Shao, H. Silicon-Based Lithium Ion Battery Systems: State-of-the-Art from Half and Full Cell Viewpoint. *Adv. Funct. Mater.* **2021**, *31* (34), 2102546.
- (7) Feng, K.; Li, M.; Liu, W.; Kashkooli, A. G.; Xiao, X.; Cai, M.; Chen, Z. Silicon-Based Anodes for Lithium-Ion Batteries: From Fundamentals to Practical Applications. *Small* **2018**, *14* (8), 1702737.
- (8) Tang, J.; Wu, F.; Dai, X.; Zhou, J.; Pang, H.; Duan, X.; Xiao, B.; Li, D.; Long, J. Robust MXene adding enables the stable interface of silicon anodes for high-performance Li-ion batteries. *Chem. Eng. J.* **2023**, *452*, 139139.
- (9) Wu, X.; Lan, X.; Hu, R.; Yao, Y.; Yu, Y.; Zhu, M. Tin-Based Anode Materials for Stable Sodium Storage: Progress and Perspective. *Adv. Mater.* **2022**, *34* (7), No. e2106895.
- (10) Zhou, J.; Shi, Q.; Ullah, S.; Yang, X.; Bachmatiuk, A.; Yang, R.; Rummeli, M. H. Phosphorus-Based Composites as Anode Materials for Advanced Alkali Metal Ion Batteries. *Adv. Funct. Mater.* **2020**, *30* (49), 2004648.
- (11) Chang, G.; Zhao, Y.; Dong, L.; Wilkinson, D. P.; Zhang, L.; Shao, Q.; Yan, W.; Sun, X.; Zhang, J. A review of phosphorus and phosphides as anode materials for advanced sodium-ion batteries. *J. Mater. Chem. A* **2020**, *8* (10), 4996–5048.
- (12) Kim, H.-H.; Kim, K.-H.; Hong, S.-H. Anion exchanged NiP_{2-x}S_x solid solution as an anode for sodium ion battery. *Chem. Eng. J.* **2023**, *455*, 140798.

- (13) He, Y.; Jiang, L.; Chen, T.; Xu, Y.; Jia, H.; Yi, R.; Xue, D.; Song, M.; Genc, A.; Bouchet-Marquis, C.; et al. Progressive growth of the solid-electrolyte interphase towards the Si anode interior causes capacity fading. *Nat. Nanotechnol.* **2021**, *16* (10), 1113–1120.
- (14) Wang, L.; Świątowska, J.; Dai, S.; Cao, M.; Zhong, Z.; Shen, Y.; Wang, M. Promises and challenges of alloy-type and conversion-type anode materials for sodium–ion batteries. *Mater. Today Energy* **2019**, *11*, 46–60.
- (15) Jin, H.; Wang, H.; Qi, Z.; Bin, D.-S.; Zhang, T.; Wan, Y.; Chen, J.; Chuang, C.; Lu, Y.-R.; Chan, T.-S.; Ju, H.; et al. A Black Phosphorus–Graphite Composite Anode for Li-/Na-/K-Ion Batteries. *Angew. Chem., Int. Ed.* **2020**, *59*, 2318–2322.
- (16) Wu, S.; Hui, K. S.; Hui, K. N. 2D Black Phosphorus: from Preparation to Applications for Electrochemical Energy Storage. *Adv. Sci.* **2018**, *5* (5), 1700491.
- (17) Cheng, J.; Gao, L.; Li, T.; Mei, S.; Wang, C.; Wen, B.; Huang, W.; Li, C.; Zheng, G.; Wang, H.; Zhang, H. Two-Dimensional Black Phosphorus Nanomaterials: Emerging Advances in Electrochemical Energy Storage Science. *Nano-Micro Lett.* **2020**, *12* (1), 179.
- (18) Jin, H.; Xin, S.; Chuang, C.; Li, W.; Wang, H.; Zhu, J.; Xie, H.; Zhang, T.; Wan, Y.; Qi, Z.; et al. Black Phosphorus Composites with Engineered Interfaces for High-rate High-capacity Lithium storage. *Science* **2020**, *370*, 192–197.
- (19) Zhang, S.; Zhang, Y.; Zhang, Z.; Wang, H.; Cao, Y.; Zhang, B.; Liu, X.; Mao, C.; Han, X.; Gong, H.; Yang, Z.; Sun, J. Bi Works as a Li Reservoir for Promoting the Fast-Charging Performance of Phosphorus Anode for Li-Ion Batteries. *Adv. Energy Mater.* **2022**, *12*, 2103888.
- (20) Hembram, K. P. S. S.; Jung, H.; Yeo, B. C.; Pai, S. J.; Kim, S.; Lee, K.-R.; Han, S. S. Unraveling the Atomistic Sodiation Mechanism of Black Phosphorus for Sodium Ion Batteries by First-Principles Calculations. *J. Phys. Chem. C* **2015**, *119* (27), 15041–15046.
- (21) Hembram, K. P.; Jung, H.; Yeo, B. C.; Pai, S. J.; Lee, H. J.; Lee, K. R.; Han, S. S. A comparative first-principles study of the lithiation, sodiation, and magnesiation of black phosphorus for Li-, Na-, and Mg-ion batteries. *Phys. Chem. Chem. Phys.* **2016**, *18* (31), 21391–21397.
- (22) Ming, J.; Cao, Z.; Wu, Y.; Wahyudi, W.; Wang, W.; Guo, X.; Cavallo, L.; Hwang, J.-Y.; Shamim, A.; Li, L.-J.; et al. New Insight on the Role of Electrolyte Additives in Rechargeable Lithium Ion Batteries. *ACS Energy Lett.* **2019**, *4* (11), 2613–2622.
- (23) Haregewoin, A. M.; Wotango, A. S.; Hwang, B.-J. Electrolyte additives for lithium ion battery electrodes: progress and perspectives. *Energy Environ. Sci.* **2016**, *9* (6), 1955–1988.
- (24) Shi, Y.; Zhou, X.; Yu, G. Material and Structural Design of Novel Binder Systems for High-Energy, High-Power Lithium-Ion Batteries. *Acc. Chem. Res.* **2017**, *50* (11), 2642–2652.
- (25) Zhao, H.; Wei, Y.; Wang, C.; Qiao, R.; Yang, W.; Messersmith, P. B.; Liu, G. Mussel-Inspired Conductive Polymer Binder for Si-Alloy Anode in Lithium-Ion Batteries. *ACS Appl. Mater. Interfaces* **2018**, *10* (6), 5440–5446.
- (26) Liu, D.; Zhao, Y.; Tan, R.; Tian, L.-L.; Liu, Y.; Chen, H.; Pan, F. Novel conductive binder for high-performance silicon anodes in lithium ion batteries. *Nano Energy* **2017**, *36*, 206–212.
- (27) Li, Z.; Zhang, Y.; Liu, T.; Gao, X.; Li, S.; Ling, M.; Liang, C.; Zheng, J.; Lin, Z. Silicon Anode with High Initial Coulombic Efficiency by Modulated Trifunctional Binder for High-Areal-Capacity Lithium-Ion Batteries. *Adv. Energy Mater.* **2020**, *10* (20), 1903110.
- (28) Zhao, F.; Deng, W.; Dong, D.; Zhou, X.; Liu, Z. Seamlessly integrated alloy-polymer interphase for high-rate and long-life lithium metal anodes. *Mater. Today Energy* **2022**, *26*, 100988.
- (29) Zoller, F.; Härlinger, S.; Böhm, D.; Illner, H.; Döblinger, M.; Sofer, Z.; Finsterbusch, M.; Bein, T.; Fattakhova-Rohlfing, D. Overcoming the Challenges of Freestanding Tin Oxide-Based Composite Anodes to Achieve High Capacity and Increased Cycling Stability. *Adv. Funct. Mater.* **2021**, *31* (43), 2106373.
- (30) Zhu, Z.; Pei, Z.; Liu, B.; Sun, D.; Fang, Y.; Lei, X.; Liu, X.; Niu, S.; Pan, H.; Zhou, J.; Qian, Y.; Wang, G. Hierarchical Ion/Electron Networks Enable Efficient Red Phosphorus Anode with High Mass Loading for Sodium Ion Batteries. *Adv. Funct. Mater.* **2022**, *32*, 2110444.
- (31) Li, B.; Song, Y.; Wang, Y.; He, Z.; Gao, W. Yolk-shelled SnO₂@NxC spheres with controllable void space as high-capacity and cycle-stable anode materials for Lithium-ion batteries. *Mater. Design* **2022**, *219*, 110745.
- (32) Zhang, Y.; Sun, W.; Luo, Z.-Z.; Zheng, Y.; Yu, Z.; Zhang, D.; Yang, J.; Tan, H. T.; Zhu, J.; Wang, X.; et al. Functionalized few-layer black phosphorus with super-wettability towards enhanced reaction kinetics for rechargeable batteries. *Nano Energy* **2017**, *40*, 576–586.
- (33) Abellán, G.; Neiss, C.; Lloret, V.; Wild, S.; Chacon-Torres, J. C.; Werbach, K.; Fedi, F.; Shiozawa, H.; Gorling, A.; Peterlik, H.; et al. Exploring the Formation of Black Phosphorus Intercalation Compounds with Alkali Metals. *Angew. Chem., Int. Ed. Engl.* **2017**, *56* (48), 15267–15273.
- (34) Kim, S.; Cui, J.; Dravid, V. P.; He, K. Orientation-Dependent Intercalation Channels for Lithium and Sodium in Black Phosphorus. *Adv. Mater.* **2019**, *31* (46), 1904623.
- (35) Lu, H.; Xu, B.; Shi, J.; Wu, M.; Hu, Y.; Ouyang, C. Structural, electronic, sodium diffusion and elastic properties of Na–P alloy anode for Na-ion batteries: Insight from first-principles calculations. *Mod. Phys. Lett. B* **2016**, *30* (32n33), 1650385.
- (36) Choi, Y.-S.; Scanlon, D. O.; Lee, J. C. Extending the Performance Limit of Anodes: Insights from Diffusion Kinetics of Alloying Anodes. *Adv. Energy Mater.* **2020**, *11* (27), 2003078.
- (37) Perdew, J. P.; Ernzerhof, M.; Burke, K. Rationale for mixing exact exchange with density functional approximations. *J. Chem. Phys.* **1996**, *105* (22), 9982–9985.
- (38) Kresse, G.; Furthmüller, J. Efficient iterative schemes for ab initio total-energy calculations using a plane-wave basis set. *Phys. Rev. B* **1996**, *54* (16), 11169.
- (39) Belsky, A.; Hellenbrandt, M.; Karen, V. L.; Luksch, P. New Developments in the Inorganic Crystal Structure Database (ICSD): Accessibility in Support of Materials Research and Design. *Acta Crystallogr. B Struct. Sci.* **2002**, *58*, 364–369.
- (40) Jain, A.; Ong, S. P.; Hautier, G.; Chen, W.; Richards, W. D.; Dacek, S.; Cholia, S.; Gunter, D.; Skinner, D.; Ceder, G.; Persson, K. A. Commentary: The Materials Project: A materials genome approach to accelerating materials innovation. *APL Mater.* **2013**, *1*, 011002.
- (41) Nose, S. Constant temperature molecular dynamics method. *Prog. Theor. Phys. Suppl.* **1991**, *103*, 1.
- (42) Ong, S. P.; Mo, Y.; Richards, W. D.; Miara, L.; Lee, H. S.; Ceder, G. Phase stability, electrochemical stability and ionic conductivity of the Li₁₀ ± 1MP2 × 12 (M = Ge, Si, Sn, Al or P, and X = O, S or Se) family of superionic conductors. *Energy Environ. Sci.* **2013**, *6* (1), 148–156.
- (43) He, X.; Zhu, Y.; Mo, Y. Origin of fast ion diffusion in superionic conductors. *Nat. Commun.* **2017**, *8*, 15893.
- (44) He, X.; Zhu, Y.; Epstein, A.; Mo, Y. Statistical variances of diffusional properties from ab initio molecular dynamics simulations. *Npj Comput. Mater.* **2018**, *4* (1), 18.
- (45) Deng, Z.; Zhu, Z.; Chu, I.-H.; Ong, S. P. Data-Driven First-Principles Methods for the Study and Design of Alkali Superionic Conductors. *Chem. Mater.* **2017**, *29* (1), 281–288.
- (46) Perez, F.; Granger, B. E. IPython: A System for Interactive Scientific Computing. *Comput. Sci. Eng.* **2007**, *9*, 21–29.
- (47) Henkelman, G.; Uberuaga, B. P.; Jónsson, H. A climbing image nudged elastic band method for finding saddle points and minimum energy paths. *J. Chem. Phys.* **2000**, *113* (22), 9901–9904.
- (48) Madsen, G. K. H.; Singh, D. J. BoltzTraP: A code for calculating band-structure dependent quantities. *Comput. Phys. Commun.* **2006**, *175* (1), 67–71.
- (49) Bardeen, J.; Shockley, W. Deformation Potentials and Mobilities in Non-Polar Crystals. *Phys. Rev.* **1950**, *80* (1), 72–80.
- (50) Xi, J.; Long, M.; Tang, L.; Wang, D.; Shuai, Z. First-principles prediction of charge mobility in carbon and organic nanomaterials. *Nanoscale* **2012**, *4* (15), 4348–4369.
- (51) McDowell, M. T.; Lee, S. W.; Nix, W. D.; Cui, Y. 25th anniversary article: Understanding the lithiation of silicon and other

alloying anodes for lithium-ion batteries. *Adv. Mater.* **2013**, *25* (36), 4966–4985.

(52) Xia, W.; Zhang, Q.; Xu, F.; Ma, H.; Chen, J.; Qasim, K.; Ge, B.; Zhu, C.; Sun, L. Visualizing the Electrochemical Lithiation/Delithiation Behaviors of Black Phosphorus by in Situ Transmission Electron Microscopy. *J. Phys. Chem. C* **2016**, *120* (11), 5861–5868.

(53) Bai, Q.; Yang, L.; Chen, H.; Mo, Y. Computational Studies of Electrode Materials in Sodium-Ion Batteries. *Adv. Energy Mater.* **2018**, *8* (17), 1702998.

(54) Gao, Y.; Nolan, A. M.; Du, P.; Wu, Y.; Yang, C.; Chen, Q.; Mo, Y.; Bo, S.-H. Classical and Emerging Characterization Techniques for Investigation of Ion Transport Mechanisms in Crystalline Fast Ionic Conductors. *Chem. Rev.* **2020**, *120* (13), 5954–6008.

(55) Van der Ven, A.; Deng, Z.; Banerjee, S.; Ong, S. P. Rechargeable Alkali-Ion Battery Materials: Theory and Computation. *Chem. Rev.* **2020**, *120* (14), 6977.

(56) Chen, D.; Jie, J.; Weng, M.; Li, S.; Chen, D.; Pan, F.; Wang, L.-W. High throughput identification of Li ion diffusion pathways in typical solid state electrolytes and electrode materials by BV-Ewald method. *J. Mater. Chem. A* **2019**, *7* (3), 1300–1306.